Manufacturing of W/steel composites using electro-discharge sintering process

Vishnu Ganesh [a,b,*], Lennart Leich [b], Daniel Dorow-Gerspach [a], Simon Heuer [a], Jan Willem Coenen [a,d], Marius Wirtz [a], Gerald Pintsuk [a], Friedel Gormann [a], Philipp Lied [c], Siegfried Baumgärtner [c], Werner Theisen [b], Christian Linsmeier [a]

[a] *Institut für Energie- und Klimaforschung – Plasmaphysik, Forschungszentrum Jülich GmbH, Jülich 52425, Germany*
[b] *Institut für Werkstoffe, Lehrstuhl Werkstofftechnik, Ruhr-Universität Bochum, Bochum 44801, Germany*
[c] *Institute for Applied Materials – Applied Materials Physics, Karlsruhe Institute of Technology, Eggenstein-Leopoldshafen 76344, Germany*
[d] *Department of Engineering Physics, University of Wisconsin-Madison, Wisconsin 53706, USA*

ARTICLE INFO

ABSTRACT

Tungsten-steel metal matrix composites are consolidated using electro-discharge sintering. At first steel and tungsten powders are sintered separately and then 25 vol% W, 50 vol% W and 75 vol% W mixed powders are sintered. A thorough process parametric study is carried out involving analysis of the influence of particle size distribution, sintering pressure, and discharge energy on the maximum discharge current and obtained residual porosity. Thermal expansion coefficient and the specific heat capacity of the optimized sintered composites are almost same as their theoretical values, however the thermal conductivities and the mechanical properties are lower than the expected values.

1. Introduction

Tungsten (W), a refractory material with body centred cubic crystal structure, is under consideration as plasma facing material in a future fusion reactor. Its properties like low sputtering yield, low hydrogen retention, high melting point, high thermal conductivity and good heat capacity are beneficial for its use as plasma facing material for the first wall and divertor alike [1–4]. Below this material, a reduced activation ferritic/martensitic steel, like EUROFER 97, is under investigation as the structural heat sink material for the first wall [5–8]. This requires the joining of W and steel. In the case of direct joining, this leads to two major challenges. First, the coefficient of thermal expansion (CTE) of W (4.4×10^{-6}/K) and that of steel (12×10^{-6}/K) differ widely, resulting in high thermal stress peaks at their interface [6]. Second, iron (Fe) and W form brittle intermetallic compounds (IMC) at elevated temperatures [9].

A possible solution to the first challenge above is to introduce a graded W/steel composite, a so-called functionally graded material (FGM), as an interlayer, which mitigates the abrupt change of the CTE at the interface [10–12]. A possible route to make such graded W/steel composites is using powder metallurgy: hot pressing [13], resistance sintering [14] and spark plasma sintering [15,16]. But, because of the long processing time under high temperatures employed in these techniques, large amounts of IMC were found to be formed. Electro-discharge sintering (EDS) is an ultra-fast consolidation technique which is analogous to a combination of spark plasma sintering [17] and capacitor discharge welding [18]. Aluminium alloys [19–21], chromium steels [22] and nanocrystalline NdFeB magnets [23] have already been sintered using EDS.

In a first feasibility study W/Fe composites were consolidated using EDS by Heuer et al. [24]. The sintered W/Fe composites from manually mixed W/Fe powders resulted in high porosities and this large pore fraction was mainly caused by the use of irregularly shaped W powder, which contains large amounts of particle agglomerates with voids that did not consolidate. Therefore, to reduce the porosity, the Fe and W powders were energetically mixed, using ball milling, and then sintered. However, this ball milling process incorporates the formation of inter-metallic phases in the powder processing step itself which remain inside the sintered composites. Another challenge is that the microstructure of these composites from ball milled mixed powders exhibits fine lamellar Fe/W structures on very small scales which act as local stress concentration regions in theory. Therefore, in this present work spherical W

---

and steel powders were used, which do not contain such agglomerates and the mixing of these powders was carried out without ball milling.

2. Methodology of the sintering process

2.1. Powders used

Two different batches of spherical W powders were used. The first batch, with a particle size fraction (PSF) of $+30/-90$ μm and D50 of 65 μm, was bought from Tekna Powders, Canada. This powder was then sieved into two different powders with PSF of $+30/-60$ μm and $+60/-90$ μm. The other batch of spherical W powder, with PSF of $+10/-30$ μm and D50 of 18 μm, was purchased from China Tungsten Online (Xiamen) Manu. & Sales Corp. Two batches of EUROFER 97 steel powder, manufactured through gas atomization, was obtained from Nanoval GmbH & Co. KG: one batch with PSF of $+10/-20$ μm and D50 of 13 μm and another batch with PSF of $+10/-100$ μm and D50 of 36 μm.

2.2. Sintering setup

The EDS setup is shown in Fig. 1. It comprises a modified capacitor discharge welding setup from Manfred Schlemmer GmbH and a powder pressing module from Frey & Co GmbH [25]. Powder is fed into a die, which is a steel casing with Si_3N_4 lining press fitted inside it. The powder is pressed using two vertical CuCo2Be punches of 19 mm diameter, which also act as electrodes. The upper punch is vertically movable, the lower punch is fixed. A hydraulic pressing module has the capability to press the punches with a maximum force of 110 kN corresponding to a sintering pressure of 388 MPa.

The sintering process follows at first the mechanical compression of the powder. The punches are connected to a capacitor bank, which can store up to 80 kJ of electrical energy, via a step-down transformer [26,27]. When this electrical energy is discharged, a single pulse very high DC current (maximum of 300 kA) at lower electrical voltage flows within milliseconds through the compressed powder as shown in Fig. 2 [24,25]. The Si_3N_4 is an electrical insulator which ensures that the electric current flows completely through the punch and the powder. As the current flows through the compressed powder, because of the electrical resistance provided by particle-particle contact of the powder, Joule's heat is generated locally as shown in Fig. 2. In other words, the stored electrical energy is converted into Joule's heating of the powder (ignoring the energy efficiency [28]). This locally generated heat promotes the welding of the particles with each other by the formation of a liquid phase and is responsible for the metallurgical bond formation at the particle-particle interface; as reported by Schütte [22], neck formation between particles takes place and as the discharge energy increases the neck formation becomes larger and larger closing the interparticle voids. Depending on the heat generated and the pressure applied, the powders consolidates within 5 to 10 ms [23,29]. This combined effect of high sintering pressure and high discharge current
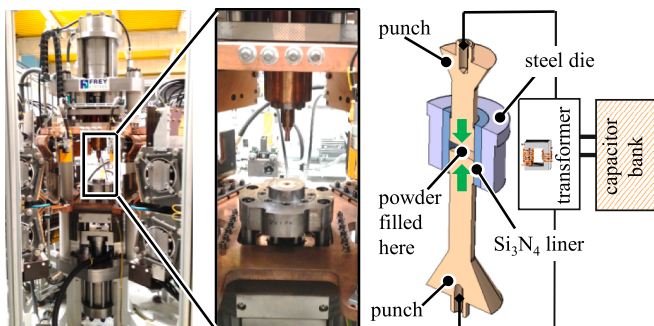
consolidates the powder [24]. The main process parameters are amount of powder, the mechanical sintering pressure and the discharge energy, which can be chosen independently.

As mentioned by Leich [23] and Orru [30] the number of scientific publications on the EDS process is lower than the well-known spark plasma sintering (SPS) process. Therefore some differences in the working principle between these two processes are explained here. In the case of EDS, since the consolidation takes place within milliseconds, there is no need for a controlled atmosphere unlike in SPS [22,24]. In the case of SPS, a continuous pulsed DC current (generally) of several kA flows through the powder [31], whereas in EDS a single pulse electric DC current of magnitude greater than 200 kA flows. In the case of SPS (with a fixed pulse ON/OFF time), the input sintering parameters (generally) are sintering temperature, sintering time and sintering pressure whereas in the case of EDS, the input parameters are electrical discharge energy and sintering pressure. In the case of SPS, the PID controller regulates the DC current amplitude to achieve the mentioned temperature. So in the case of SPS, the amount of total theoretical electrical input energy can be vaguely calculated by multiplying DC current amplitude, voltage, sintering time and the ratio of pulse ON time to total cycle time. This input energy is not fixed, whereas in the case of EDS process, the total energy is a fixed input parameter and the discharge current is a result of the electrical resistance of the powder.

The EDS setup in the present study is equipped to measure the discharge current and the upper punch displacement during a sintering experiment. The discharge current and the punch displacement for one such sintering experiment (for 100 vol% steel) is shown in Fig. 3, including some important parameters of the consolidation process.

2.3. Sintering procedure

The powder to be sintered was first weighed to produce a 3 mm thick sintered disc of diameter 19 mm (assuming no residual porosity). An
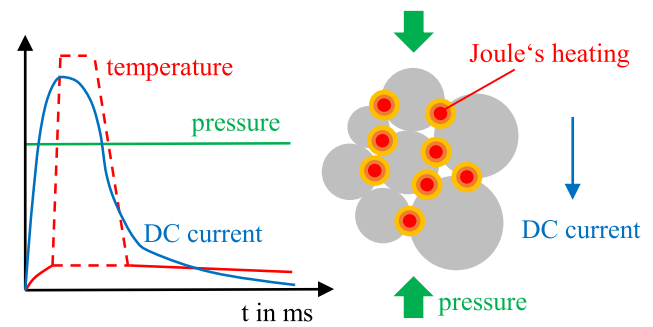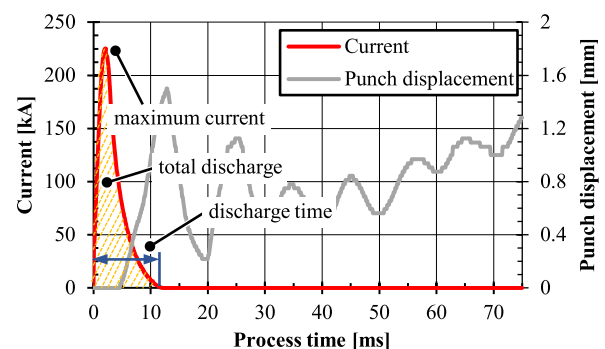
Fig. 2. Schematic representation of current, temperature and pressure profile during a typical electro-discharge consolidation [25] and the generation of Joule's heating at the particle contacts.

Fig. 1. Equipment for EDS process and the corresponding schematic diagram.

Fig. 3. An exemplary profile of discharge current and relative displacement of the punch.

exemplary macroscopic image of such a consolidated disc is shown in Fig. 4.

Before the sintering of W/steel powders, first steel and W powders were sintered separately to understand the behaviour of the sintering setup. Steel powders were first sieved into powders of different PSF and then sintered to study the effect of particle size on the densities of the consolidates. At first the steel powders were sintered at 388 MPa and 60 kJ energy and upon successful sintering fresh powders were sintered at 80 kJ energy. As reported by Heuer et al. [24], around 0.3 mm thick material on the top and bottom of the specimens are not fully sintered, and this is usually the case with EDS [22,32,33]. Likewise, the three sieved W powders with PSF (+10/−30 μm, +30/−60 μm and +60/−90 μm), were tested to consolidate at 388 MPa with 80 kJ. Only the W powder with PSF +10/−30 μm showed some densification whereas the others remained as raw powders.

For mechanical reasons (particularly ductility), the W/steel composites should have steel as the matrix with W as the embedded particles. Although generally in MMCs the reinforcing particles should be finer and well dispersed within the matrix, but in the case of W/steel-composites the W particles are not intended to strengthen the matrix but to achieve the desired CTE. The W particles represent rather a weak spot because at the interface between W and steel a brittle intermetallic phase forms. By using fewer but larger particles, a lower amount of these intermetallics will be present. Also, employing finer W particles would increase the probability of two particles touching each other and this might result in several non-sintered W-W particles thereby, weakening the mechanical stability. Therefore, for the present W/steel-composites the steel particles should be finer than the W particles; but the particle size choice is not completely free due to the sintering process and based on the results of the sintering of 100 vol% steel powders with different PSF, it was evident that the sintering process substantially depends on the particle sizes of the steel powder. Therefore, a range of steel powders were selected from fine to coarse to manufacture W/steel composites. First, the W and steel powders were sieved to get the dedicated PSF and then these steel and W powders, weighing according to the desired volume concentration of W, were filled in a plastic jar. The jar was closed and sealed inside argon atmosphere and subsequently mixed using a tumble mixer for 48 h. All mixed powders were then sintered at a variety of sintering pressures and discharge energies. The complete set of experimental parameters and the obtained outcomes with different composition are provided in Table 1.

The primary objective for the variety of process parameters (PSF, pressure and discharge energy) was to investigate their effects on the discharge parameters as well as on the porosity of the sintered composites. The porosity of the consolidated samples was measured using quantitative image analysis. The samples were cut along two different planes as depicted in Fig. 4 and metallographic investigations were performed on these cross-sectional planes. For each parameter one composite was sintered and 15–20 scanning electron microscopy (SEM) images were taken at different locations with different magnifications to include micro- as well as meso–scale voids. Their mean is presented here
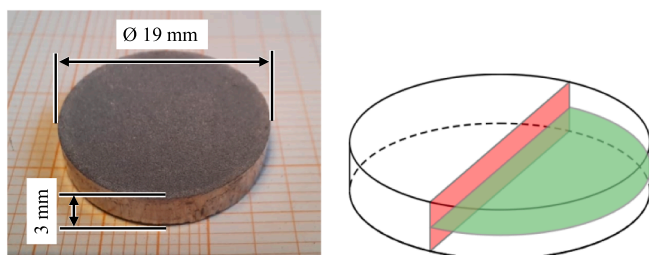

Fig. 4. A sintered disc and cutting planes of the sintered geometry (red and green) for porosity analysis. (For interpretation of the references to colour in this figure legend, the reader is referred to the web version of this article.)

Table 1
Overview of the composition for 25 vol% W, 50 vol% W and 75 vol% W made from different PSF, sintered at different pressure and discharge energy and their corresponding outcome.

Composition*	Sintering pressure (MPa)	Discharge energy (kJ)	Remark
$25W_{10-30}+75S_{40-100}$	388; 317; 247; 176	40; 60; 80	sintered
$25W_{10-30}+75S_{10-40}$	388	80	welded with electrode
$25W_{10-30}+75S_{10-20}$	388	80	welded with electrode
$25W_{30-60}+75S_{40-100}$	388; 317; 247; 176	40; 60; 80	sintered
$25W_{30-60}+75S_{40-63}$	388	40; 60; 80	only sintered at 80 kJ
$25W_{30-60}+75S_{30-80}$	388	40; 60; 80	welded with electrode
$25W_{30-60}+75S_{10-20}$	388	80	welded with electrode
$50W_{10-30}+50S_{10-20}$	388	80	welded with electrode
$50W_{30-60}+50S_{40-100}$	388; 317; 247	40; 60; 80	sintered
$50W_{30-60}+50S_{10-20}$	388	80	welded with electrode
$50W_{60-90}+50S_{40-100}$	388; 317; 247	40; 60; 80	sintered
$50W_{60-90}+50S_{40-63}$	388	80	sintered
$50W_{60-90}+50S_{30-80}$	388	80	welded with electrode
$75W_{10-30}+25S_{40-100}$	388; 317	40; 60; 80	only the trials at 388 MPa with 80 kJ sintered properly
$75W_{30-60}+25S_{40-100}$	388; 317	40; 60; 80	
$75W_{60-90}+25S_{40-100}$	388; 317	40; 60; 80	
$75W_{80-90}+25S_{40-100}$	388; 317	40; 60; 80	

(*: the subscript represents the PSF, for e.g., $25W_{10-30}+75S_{40-100}$ means a composite with 25 vol% tungsten made from tungsten powder of PSF+10/−30 μm and corresponding for its steel constituent).

as average porosity of the sintered composite and the calculated standard deviation represents the error band.

2.4. Mechanical characterization

A miniature 4-point bending test was conducted on the optimized consolidated composites at 20 °C, 100 °C (in air), 300 °C (in air), and 550 °C (under vacuum). The load span was 5 mm apart and the support span was 10 mm apart with 1 mm diameter supports. The crosshead speed was kept at 0.033 mm/min. Bending specimens (1 mm ×1 mm ×12 mm) were cut using wire electrical discharge machining (EDM). The flexural stress at the outermost surface and the flexural strain were calculated based on the formulae provided in ASTM D7264/D7264M [34].

2.5. Thermophysical characterization

The thermophysical characterizations were also performed on specimens cut using wire-EDM from each optimized consolidated compositions. The characterizations were carried out on "as sintered" state as well as on "heat treated" state: for heat treatment the sintered specimens were held (inside vacuum oven) at 1000 °C for 30 min for austenization annealing of the steel and then cooled down. After that, they were held (inside vacuum oven) at 760 °C for 90 min for tempering according to the parameters presented for EUROFER 97 steel [6].

2.5.1. Dilatometer studies

Dilatometer test was performed on 4 mm ×2 mm ×15 mm specimens under Ar atmosphere using a vertical double-specimen dilatometer LV75 from LINSEIS at a constant heating rate of 4 K/min from 20 °C to 1000 °C.

2.5.2. Dynamic differential scanning calorimetry (DSC) studies

The specific heat capacity (c_p) was measured on Ø 5 mm ×1.5 mm specimens using NETZSCH DSC 404 F3 system under Ar atmosphere using platinum crucible from 20 °C to 1000 °C at a heating rate of 20 K/min.

2.5.3. Laser flash analysis (LFA) studies

The thermal diffusivity (a) was measured using NETZSCH LFA 427 laser flash analysis system on 10 mm ×10 mm ×1.5 mm specimens between 20 °C and 1000 °C at an interval of 200 °C. The thermal conductivity (λ) was then calculated by multiplying density (measured using Archimedes' principle), specific heat capacity and thermal diffusivity.

3. Results and discussion

3.1. Separate sintering of steel powder

The maximum discharge current during the sintering and the residual porosities of the sintered steel specimen from powders of different PSF are shown in Fig. 5.

The least porosity is obtained for the sintering which corresponds to highest maximum discharge current. The maximum discharge current tends to be higher for the PSF with coarser particles and it behaves somewhat inverse to the obtained residual porosities. The discharge time showed no significant variation and also the total discharge showed a similar pattern like the maximum discharge current. Powders with coarse particles sintered better and resulted in lower porosities as compared to finer powders. In conventional sintering finer particles cause faster diffusion and lead to higher densities. However, in EDS this is not observed, this behaviour could be understood by the following explanation:

- Firstly, as reported by Leich [28], the electrical potential (V) remains almost the same for all the consolidations. Since the measured discharge current (I) is lower for powders with smaller particles, the overall electrical resistance (R) of finer powders must be higher than that of coarser powders. This can be understood on the basis of contact resistance of a steel-steel particle contact. As the finer powder exhibit higher number of such contact points as that of the coarser powder, the overall re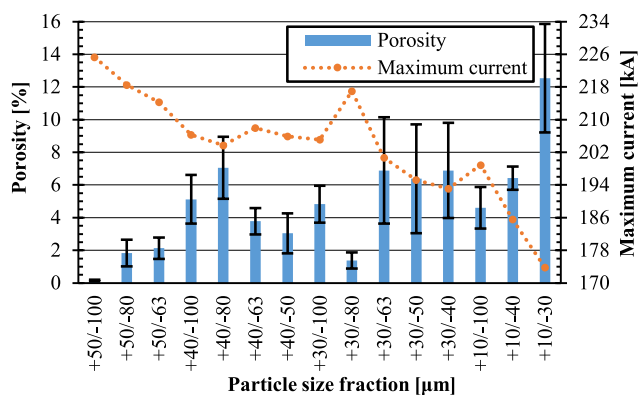sistance (R) would be higher as that of the coarser powder. Since the electrical discharge energy is the same for both these powders, a lower current flows through the finer powder as seen in Fig. 5. Such behaviour was also observed by Clyens et al. [33].

- Secondly, as the current flowing through the finer powder is lower, the Joule's heat generated at each of such steel-steel particle contact is lower in finer powder as compared to coarser powder. In other words, the given energy is dissipated among contact points; therefore, the energy dissipated locally is lower in finer powder as compared to a coarser powder, resulting in locally lower temperatures and thus leading to worse sintering.

Thus, sintering finer powder results in higher porosity, as can be seen in Fig. 6(a). The particles of fine powder only combine with other particles at their surface resulting in large voids, whereas coarser powder led to a much lower porosity (shown in Fig. 6(b)).

Based on the results observed from sintering of 100 vol% steel, it was learned that in order to obtain lower porosity a coarse steel powder should be used. However, the influence of the addition of W powder to the steel powder on their sintering behaviour was not clear. Therefore, as mentioned in Table 1, instead of only mixing a coarse steel powder with different W powders, most of the different particle sizes of W as well as steel powder were mixed to sinter W/steel-composites.

3.2. Consolidation of W/steel mixed powders

3.2.1. 25 vol% W powder

Only W/steel mixed powder made from the steel powder with coarse PSF of +40/−100 μm sintered properly, and the other mixtures with finer steel powders welded to the electrodes (see Table 1). The exact reason, why only the composition with coarser steel powder of PSF +40/−100 μm led to proper sintering is not clear, but some possible hypothesis could be made. Firstly, the W particles have higher thermal and electrical conductivity and hence the discharge is concentrated in these particles, leading to an inhomogeneous heating which is not present in the pure steel case before. This results in lesser heat generation among the steel particles. Secondly, the electrical discharge energy is insufficient to sinter W particles themselves properly. Thirdly, the probability that the discharge current flows mainly through the W particles is relatively low if the particle size of steel is greater than that of W for a given volume fraction. However, the full explanation for the welding of compositions with smaller PSF with the electrode is not yet known.

As can be seen in Fig. 7(a), an increase of the discharge energy increases linearly the maximum discharge current and results in a decrease of the average porosity. Similarly, the increase in consolidation pressure also decreases the porosity. The increase in maximum discharge current follows a sort of logarithmic pattern with respect to the pressure and a coarser W powder results in higher discharge current as seen in Fig. 7(b). However, for $25W_{30-60}+75S_{40-100}$ there was no significant decrease in the porosity above 317 MPa. Sintering of the
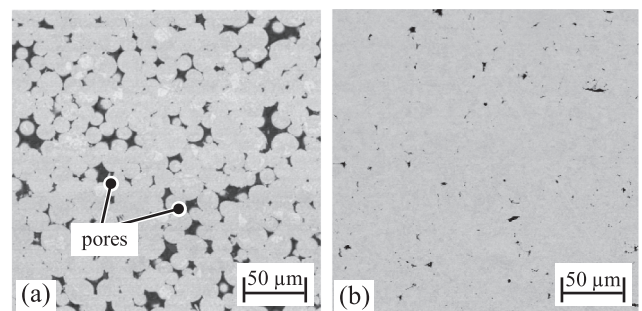
Fig. 5. Porosity and maximum discharge current measured during the sintering of 100 vol% steel under 388 MPa pressure with 80 kJ discharge energy for various particle size fraction.

Fig. 6. SEM images of sintered steel powders with PSF of (a) +10/−30 μm and (b) +40/−100 μm.
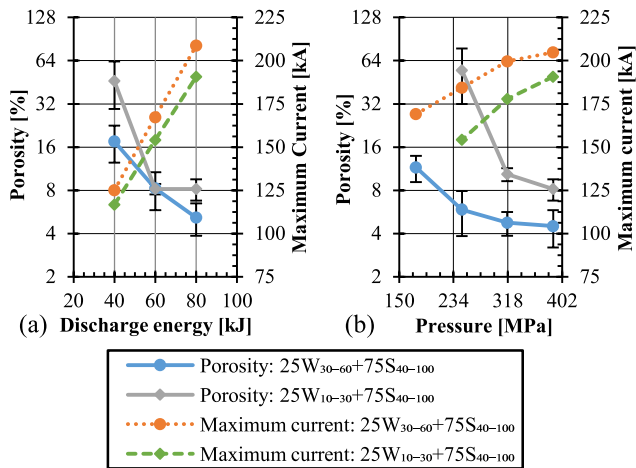
Fig. 7. Average porosity and maximum discharge current measured during the sintering of $25W_{30-60}+75S_{40-100}$ and $25W_{10-30}+75S_{40-100}$ at (a) various discharge energy at a pressure of 388 MPa and (b) various consolidation pressure with discharge energy of 80 kJ.

Fig. 9. Average porosity and maximum discharge current measured during the consolidation of $50W_{30-60}+50S_{40-100}$ and $50W_{60-90}+50S_{40-100}$ at (a) various discharge energy at a pressure of 388 MPa and (b) various consolidation pressure with discharge energy of 80 kJ.

composition with coarser W powder resulted in higher discharge current as seen in Fig. 7, which is in line with the results of sintering steel (see Fig. 4).

Cross sections of the sintered composites $25W_{10-30}+75S_{40-100}$ and $25W_{30-60}+75S_{40-100}$ are shown in Fig. 8. Voids are predominantly present in the steel matrix with embedded nearly unaltered spherical W particles, which indicates that the fraction of the discharge current preferably flows through specific W-rich paths resulting in poor consolidation in steel particles.

Another composition $25W_{30-60}+75S_{40-63}$ (not shown here) only consolidated properly at 388 MPa with 80 kJ energy but produced a porosity of around 13 %. Therefore, the $25W_{30-60}+75S_{40-100}$ will be used as the 25 vol% W sublayer inside the FGM in the future because of its least amount of porosity.

3.2.2. 50 vol% W powder

For this W/steel combination too, the mixture with coarse steel powder consolidated better than that with the finer steel powder. The powder with finer steel constituent welded to the electrode as in the 25 vol% W composition. Likewise, in the 50 vol% W case, the increase of the discharge energy led to a better densification (shown in Fig. 9(a)). As can be seen in Fig. 9(b), for the $50W_{30-60}+50S_{40-100}$ composite, the porosity decreased substantially as the pressure increased from 317 MPa to 388 MPa. However, for the $50W_{60-90}+50S_{40-100}$ composite the porosity remained almost constant. On the other hand, the discharge current showed no dependence on the particle size of the W constituent. Another composition, $50W_{60-90}+50S_{40-63}$ (not shown here), only
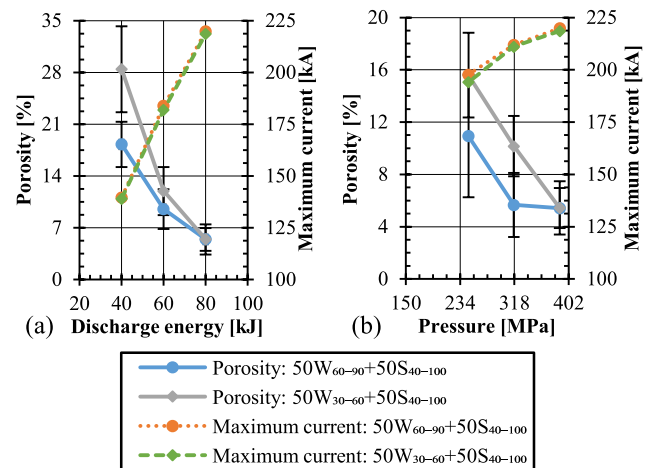
consolidated properly at the 388 MPa and 80 kJ but produced a porosity of around 15 %.

The cross section of the sintered composite with the least amount of porosity is shown in Fig. 10. Fig. 11(a) shows the magnified SEM images of various W particles together inside the $50W_{30-60}+50S_{40-100}$ composition which did not come in contact with each other to initiate any metallurgical bond formation among them. Such locations are also found in $50W_{60-90}+50S_{40-100}$ composition. Fig. 11(b and c) shows the W-W interface in some locations for the $50W_{30-60}+50S_{40-100}$ and $50W_{60-90}+50S_{40-100}$ compositions respectively. This shows two W particles, even though in close contact with each other, not forming any metallurgical bonding among them. And there also exists locations were W-W particles form a very good metallurgical bond as shown in Fig. 11(d). It must be noted that such non sintered W-W interfaces are present in few locations in both the compositions; therefore, although both the compositions ($50W_{30-60}+50_{40-100}$ and $50W_{60-90}+50_{40-100}$) exhibited the same porosity after sintering at 388 MPa with 80 kJ energy, the composition $50W_{60-90}+50_{40-100}$ is potentially better suited for the usage as 50 vol% W sublayer inside the FGM because it has a smaller number of W particles resulting in a smaller number of not-sintered W-W interfaces.

3.2.3. 75 vol% W powder

The sintering of 75 vol% W powder only resulted in some densification at the maximum available settings, 388 MPa and 80 kJ. The resulting porosity and maximum discharge current observed for different particle size ratios are specified in Fig. 12.
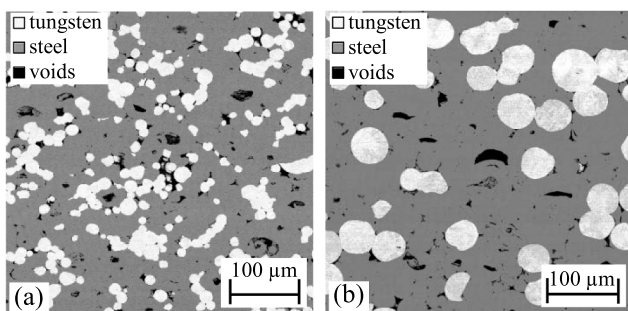

Fig. 8. Cross-section of (a) $25W_{10-30}+75S_{40-100}$ and (b) $25W_{30-60}+75S_{40-100}$ consolidated through 80 kJ discharge energy at the pressure of 388 MPa.
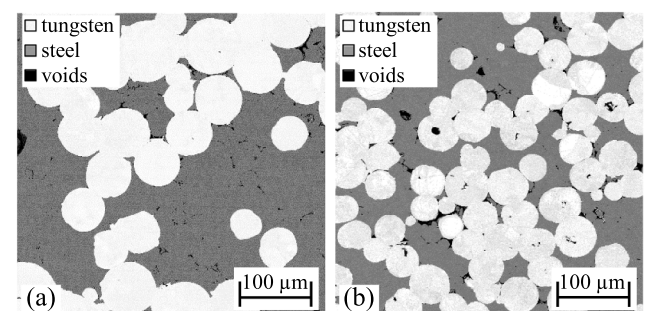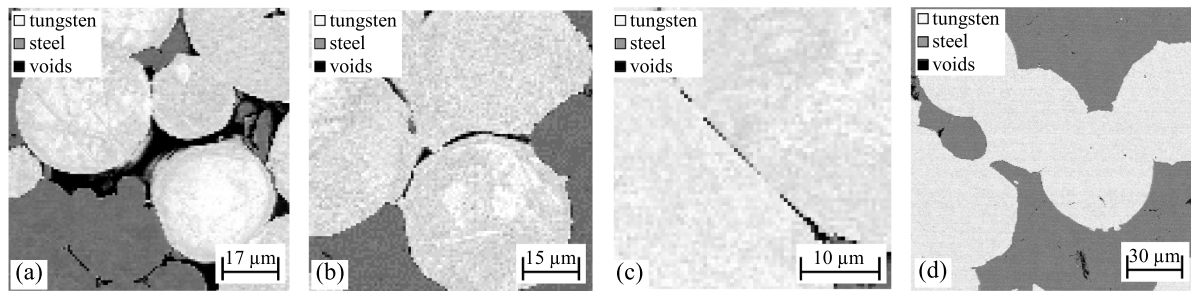

Fig. 10. Cross-section of (a) $50W_{60-90}+50S_{40-100}$ and (b) $50W_{30-60}+50S_{40-100}$ consolidated through 80 kJ discharge energy at the pressure of 388 MPa.

Fig. 11. (a) SEM image of a location in $50W_{30-60}+50S_{40-100}$ showing W particles together, (b) SEM image of a location in $50W_{30-60}+50S_{40-100}$ showing the interface between W particles, (c) SEM image of a location in $50W_{60-90}+50S_{40-100}$ showing the interface between two W particles resulting in poor metallurgical bonding among them, and (d) SEM image of a location in $50W_{60-90}+50S_{40-100}$ showing good metallurgical bonding for W-W interfaces.
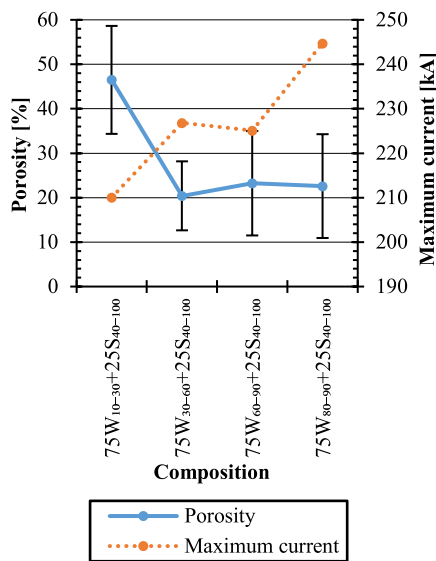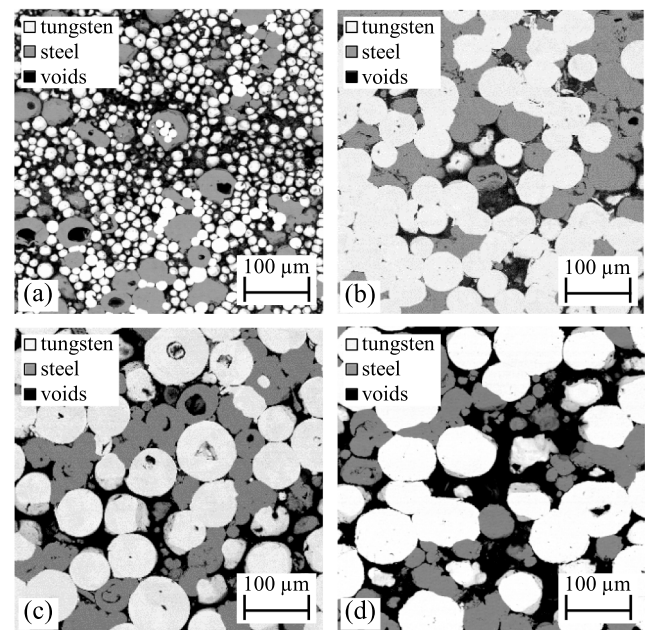

Fig. 12. Average porosity and maximum discharge current measured during the consolidation of 75 vol% W powder at 388 MPa and 80 kJ.

Fig. 13. Cross section of (a)$75W_{10-30}+25S_{40-100}$ (b)$75W_{30-60}+25S_{40-100}$ (c) $75W_{60-90}+25S_{40-100}$ and (d)$75W_{80-90}+25S_{40-100}$ consolidated at 388 MPa with 80 kJ discharge energy.

The cross-sectional SEM images of the sintered composites are shown in Fig. 13. The discharge energy appears to be not high enough to produce a dense composite. The higher thermal conductivity, thermal capacity and melting point of W compared to steel increase the necessary energy to produce dense composites. The amount of porosity present in the 75 vol% W composite is quite high and not acceptable for its use as FGM. Thus, at the current state, EDS is not appropriate for the consolidation of composites with a volume W content of more than 50 %.

3.3. Local homogeneity of sintered composites

As the current in the EDS process can flow heterogeneously through the powder, the porosity distribution of a few composites was studied closely. As can be seen in Fig. 14, the porosity varies strongly along the cross-section, and this may be due to the heterogeneous discharge of the electric current over the surface of the specimen. The porosity at locations 1 and 3 for the 25 vol% W composite sintered at a lower pressure of 317 MPa is much lower compared to their neighbouring positions, indicating that more current had passed through these locations resulting in better densification. The comparison of location 3 and 5 for 50 vol% W composite sintered at 317 MPa reveals that even quite dense composites can have hidden regions of very high porosity. This also makes it difficult and more laborious to assess the quality of a sample. Overall, this indicates that the sintered composites locally have some porous regions. The standard deviation of the porosity distribution for the $25W_{30-60}+75S_{40-100}$ sintered at 317 MPa and 388 MPa was 1.93 and

0.91 respectively. The same for the $50W_{60-90}+50S_{40-100}$ sintered at 317 MPa and 388 MPa was 2.58 and 1.5 respectively. This indicates that although the porosity values at a high pressure of 388 MPa also scattered, but the overall distribution is a bit more homogenous. Some of the SEM-images from which the porosity distribution is analysed are provided in supplementary information (Fig. S4). The large porosity variations are also noticeable when consolidating even pure steel powders, as shown in supplementary information (Fig. S5).

3.4. Characterization of the composites

The characterization was performed on $25W_{30-60}+75S_{40-100}$ and $50W_{60-90}+50S_{40-100}$ composites consolidated at 80 kJ and 388 MPa, as these exhibited the lowest porosity. For simplicity, these composites are named here after 25 vol% W and 50 vol% W, respectively.

3.4.1. 4-point bending test

The bending tests could not be performed on 50 vol% W as it was too brittle and got fractured just after the wire-EDM cutting. Hence, the tests could only be performed on 25 vol% W composite. The flexural stress–strain curve for specimens is shown in Fig. 15(a). The composites were brittle and an increase in temperature lead to slight decrease in the
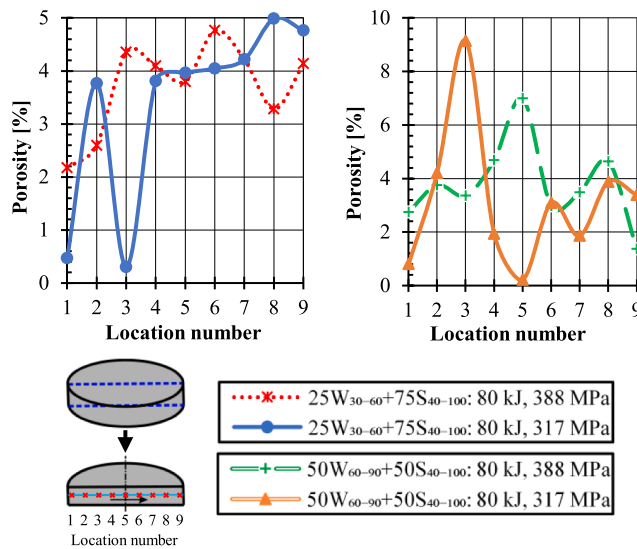
Fig. 14. Porosity distribution over the cross-section for 25 vol% W and 50 vol % W composition sintered at two different pressure.
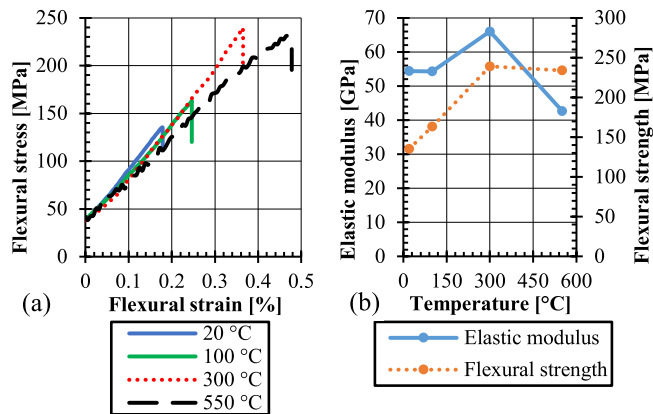

Fig. 15. (a) Flexural stress-strain curve for the 25 vol% W composites, (b) measured elastic modulus and flexural strength.

elastic modulus beyond 300 °C. The flexural strength does not increase beyond 300 °C as shown in Fig. 15(b). The theoretical elastic modulus and flexural strength, linearly interpolated from bulk values of pure W and pure steel, for a 25 vol% W composite at 20 °C are around 260 GPa and 840 MPa respectively [24]. It can be seen that the mechanical properties of the sintered composites are much lower than its theoretical counterpart.

3.4.2. Thermophysical studies

Dilatometer studies: The change in the length (ΔL) during the heating and cooling ramp of the as sintered and heat treated composites is shown in Fig. 16.

For both compositions in the as sintered state, ΔL increases linearly during the heating up to 620 °C followed by a kink in the ΔL, indicated by point 1 in Fig. 16. After the heat treatment this kink is not present anymore. For both compositions, the increase in ΔL until point 1 is almost the same for the as sintered and the heat treated specimens. After this point 1 to around 833 °C the ΔL of the as sintered specimens of both compositions decreases almost linearly. At this temperature a sudden drop occurs and this temperature refers to the austenitic start temperature indicated as γ_s [6,35]. This transformation can also be seen in the heat treated specimens but to a much smaller extent. As the austenitic
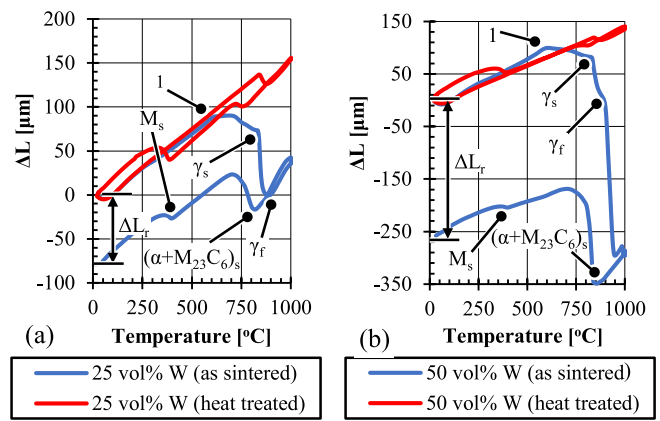

Fig. 16. Change in length under dilatometry studies for as sintered and heat treated (a) 25 vol% W composite and (b) 50 vol% W composite.

transformation occurs, the ΔL decreases because of the formation of closed packed FCC structure in the steel constituent. The austenitic transformation finishes at around 890 °C indicated as γ_f and beyond this temperature ΔL starts to increase linearly again, till the end temperature of 1000 °C [6,35]. For the as sintered 50 vol% W specimen, at a temperature slightly beyond γ_f further steep shrinkage till 920 °C was observed, after which the specimen shows the expected increase in ΔL up to 1000 °C.

Then the specimens were allowed to cool down and from the time-temperature profile the cooling rate was found to be 10 K/min. This cooling rate was found to be constant down to 300 °C and during this cooling some of the austenite transforms into ferrite and $M_{23}C_6$ carbide at around 820 °C, resulting in transitory increase of ΔL, denoted as $(\alpha + M_{23}C_6)_s$ and this transformation ends at around 720 °C [36]. As the temperature further decreases, the remaining austenite transforms into martensite at 400 °C indicated as M_s [35]. Similarly, the cooling phase in the heat treated specimens also showed these characteristic transformation temperatures. The overall length of the as sintered specimen shrinks after the cooling phase. The length difference is specified as ΔL_r. This shrinkage can be discussed based on a possible explanation: The sintered specimens have high residual porosity mainly in the steel matrix (cf. Fig. 8(b) and Fig. 10(a)). As the temperature increases beyond 620 °C, the steel matrix sinters more and closes the voids, resulting in the shrinkage of the specimen. To summarize, the ΔL of the as sintered samples exhibit three distinct differences compared to the heat treated ones

- A kink at 620 °C
- A more pronounced austenitic transition
- A large shrinkage after the austenitic transition for the 50 vol% W samples

The secant coefficient of thermal expansion (CTE) during the heating phase of the heat-treated composites is plotted in Fig. 17 and the CTE of bulk W and EUROFER 97 steel is shown for comparison [37,38]. The calculated secant CTE shows an almost linear behaviour up to 650 °C and then a slightly smaller increase. The drop in the CTE at 833 °C is due to the austenitic transformation. The CTE (α) of the composites are nearly equal to that of the theoretical values, which is calculated assuming a series model as defined in Eq. (1), where V_W is the volume concentration of W. This series model expresses a linear change in the CTE between steel and W depending on the W content and this model was employed in earlier works on W/steel-FGM to determine the theoretical CTE; therefore, the same model was used here [10–12,27,39,40]. The measured CTE of the composites agree well with the theoretical value.
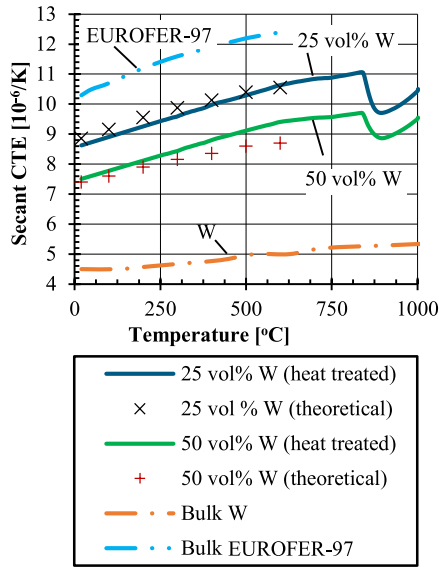
Fig. 17. Calculated secant CTE of the composites including bulk W and EUROFER 97 steel for comparison.

$$\alpha_{theoretical} = V_W\alpha_W + (1 - V_W)\alpha_{steel} \tag{1}$$

DSC studies: The measured specific heat capacity of the composites in both the states (as sintered and heat treated) is shown in Fig. 18. The c_p of bulk W and EUROFER 97 steel is shown for comparison [37,38]. The theoretical specific heat capacity ($c_{p,theoretical}$) of the composites is also depicted and it is calculated based on the Eq. (2), in which ρ and V_W are the density and volume concentration of tungsten.

$$c_{p,theoretical} = \frac{c_{p,w}\rho_W V_W + c_{p,steel}(1 - V_W)\rho_{steel}}{\rho_W V_W + (1 - V_W)\rho_{steel}} \tag{2}$$

The measured specific heat capacity of the composites are almost the same as their theoretical values showing a progressive increase up to

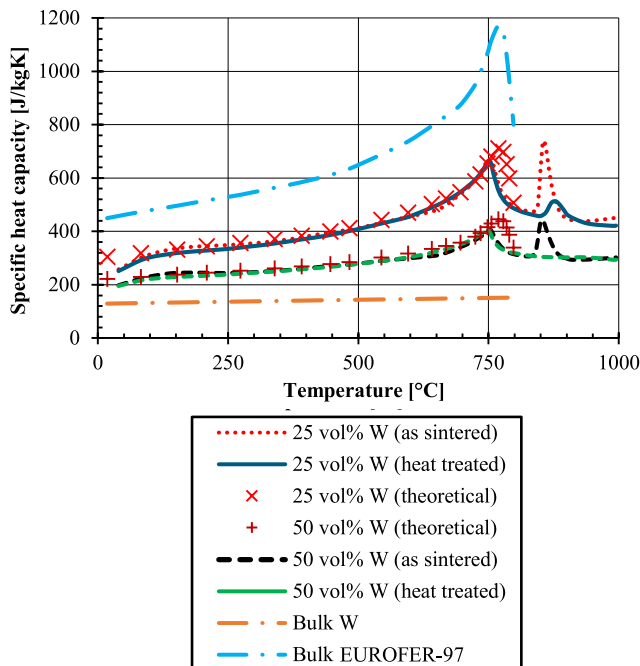**Fig. 18.** Specific heat capacity of the composites including bulk W and EUROFER 97 for comparison.

around 740 °C where the material exhibits a ferromagnetic to paramagnetic ferrite transformation as also reported by Heuer [27] and Raju et al. [41]. After that the austenitic transformation starts at around 840 °C and finishes at around 900 °C. This austenitic transformation is more pronounced in as sintered state. For 50 vol% W composite, no austenitic transformation was observed for the heat treated state, however, it should be noted that in reality austenitic transformation does occur in the heat treated 50 vol% W composite, as discussed in the dilatometer studies, but its effect on the specific heat capacity is not visible/cannot be quantified.

LFA studies: The measured thermal conductivity (λ) of the composites and the corresponding theoretical values are plotted in Fig. 19. The theoretical ($\lambda_{theoretical}$) value is calculated based on the parallel model following Eq. (3) [24]. This parallel model predicts the maximum possible theoretical thermal conductivity of such a composite and parallel model was already used for the prediction of the theoretical thermal conductivity of such W/steel-FGMs [11,27,39].

$$\lambda_{theoretical} = V_W\lambda_W + (1 - V_W)\lambda_{steel} \tag{3}$$

It can be seen that the thermal conductivities of both the composites (25 vol% W and 50 vol% W) are much lower than the theoretical expectations, which is due to the presence of residual porosity. Also, the thermal conductivity of both the conditions, as sintered and heat treated, is nearly the same, indicating that the heat treatment did not improve the quality. The thermal conductivity remains almost constant with respect to the temperature. The thermal conductivity of the 50 vol % W is lower than that of 25 vol% W. It could be due to slightly higher porosity and inferior sintering of 50 vol% W composite as compared to 25 vol% W, however, the exact reason behind this is still not known.

As mentioned above the heat treatment of the composites have led to no improvement in the thermal conductivity, although the heat treatment results in a slight reduction in the residual porosity. This implies that the residual porosity is not the main cause of the low thermal conductivity. The thermal conductivity strongly depends on the quality of the particle-particle metallurgical bonding; as mentioned earlier, some W-W particles do not form good metallurgical bonding and even after the heat treatment, there is no improvement in their bond quality as seen in the middle SEM micrograph of Fig. 20(a and b). This resulted in no improvement in the thermal conductivity of the heat-treated composites.

Also, as shown in Fig. 20(a and b) the heat treatment results in a slight formation of the intermetallic at the interface between W and steel
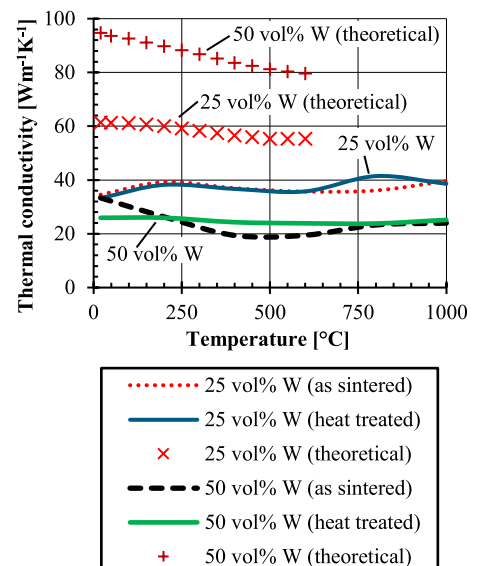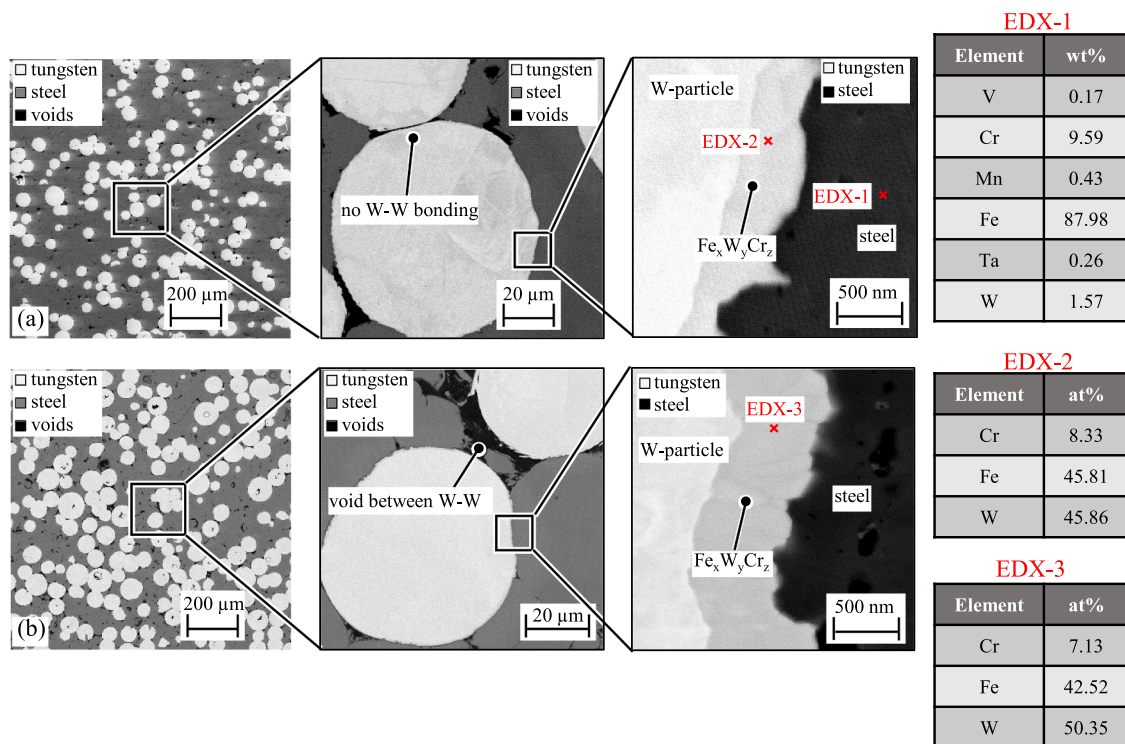

Fig. 19. Thermal conductivity of the composites.

EDX-1

Element	wt%
V	0.17
Cr	9.59
Mn	0.43
Fe	87.98
Ta	0.26
W	1.57

EDX-2

Element	at%
Cr	8.33
Fe	45.81
W	45.86

EDX-3

Element	at%
Cr	7.13
Fe	42.52
W	50.35

Fig. 20. SEM micrographs of heat treated composites: (a) $25W_{30-60}+75S_{40-100}$ and (b) $50W_{60-90}+50S_{40-100}$, with the energy dispersive X-ray (EDX) analysis at three locations.

particle and have a thickness of around 500 nm. The EDX-1 and EDX-2 analysis have shown that this intermetallic might have a complex $Fe_xW_yCr_z$ phase. The EDX analysis on the steel phase showed a similar chemical composition as that of EUROFER 97.

4. Summary and conclusion

This study investigated the feasibility to manufacture W/steel composites with three different volume concentrations of W via EDS process. These composites are supposed to be used as sublayers within a FGM, which could be used as an interlayer to join W and steel for the first wall of a fusion reactor. Spherical W and steel powders with different particle sizes were tested for the sintering process.

- The effect of PSF of the 100 vol% steel powder on the residual porosity and maximum discharge current was investigated: coarser powders result in less residual porosity and higher maximum discharge current. The sintering of 100 vol% W powder was not successful.
- The sintering of mixed W/steel powders was only successful for the mixtures containing the steel constituent with a PSF of $+40/−100$ μm and all the other mixtures with finer PSF led to the welding of the powder with the electrode.
- The residual porosity of the sintered composites decreases drastically with increasing discharge energy. The increase in the sintering pressure also decreases the residual porosity, but for certain compositions there was no significant decrease beyond 317 MPa. However, porosity distribution analysis revealed that the distribution became a bit more homogenous when sintered at the higher pressure of 388 MPa.
- The study also analysed the limits of the particle ratio of W and steel for the composites qualitatively. When the W particles are too coarse, most of the discharge current flows through the W particles resulting in no proper consolidation. If the W particles are too fine, most of the

discharge current flows through few steel particles increasing the residual porosity.
- For the 25 vol% W and the 50 vol% W, the optimum composition was found to be $25W_{30-60}+75S_{40-100}$ and $50W_{60-90}+50S_{40-100}$ respectively. Sintering at 388 MPa with 80 kJ resulted in a residual porosity of around 5 %. The discharge energy of this EDS-setup is not high enough to sinter 75 vol% W composites adequately as it resulted in very high residual porosity of 30 to 50 %.
- The CTE of the heat treated 25 vol% W and 50 vol% W composites are very close to that of theoretical CTE, illustrating the potential of these composites for the use as stress reducing interlayer. Also, the specific heat capacity of the composites calculated using DSC measurement showed a similar behaviour to that of their theoretical values. However, the thermal conductivity of the composites was much lower compared to their theoretical values, but still higher than/equal to that of EUROFER 97 steel base. This might be disadvantageous for their use as the FGM (in the first wall) since this will hinder the heat transfer, resulting in higher temperatures at the interface during the operation phase of a fusion reactor.
- The brittle behaviour of the composites and somewhat non-homogenous distribution of the porosity, due to non-uniform flow of the discharge current through the powder are further drawbacks for their usage within a FGM.
- The comprehensive experimental analysis shows that with current EDS-setup, not much improvement can be expected for the W/steel-composites: neither higher W-contents nor larger sizes of the compact are possible at the moment. However, this is not because of the EDS principle, but because of the limited discharge energy of the current setup. Conceptually, EDS-setup with higher capacitance should result in better quality of the compacts, and thereby opening up the possibility of compacting larger samples, but a larger sample size might also not make the compacts more homogenous. Nevertheless, due to the very short sintering time and comparably low energy consumption, it is still a very interesting technique.

CRediT authorship contribution statement

Vishnu Ganesh: Conceptualization, Formal analysis, Methodology, Writing – original draft. **Lennart Leich:** Formal analysis, Investigation. **Daniel Dorow-Gerspach:** Conceptualization, Investigation, Writing – review & editing. **Simon Heuer:** Validation, Methodology, Writing – review & editing. **Jan Willem Coenen:** Supervision, Funding acquisition, Resources. **Marius Wirtz:** Supervision, Funding acquisition, Resources. **Gerald Pintsuk:** Supervision, Resources. **Friedel Gormann:** Investigation. **Philipp Lied:** Investigation. **Siegfried Baumgärtner:** Investigation. **Werner Theisen:** Supervision, Resources. **Christian Linsmeier:** Project administration.

Declaration of Competing Interest

The authors declare that they have no known competing financial interests or personal relationships that could have appeared to influence the work reported in this paper.

Appendix A. Supplementary data

Supplementary data to this article can be found online at https://doi.org/10.1016/j.nme.2021.101089.

References

[1] V. Philipps, Tungsten as material for plasma-facing components in fusion devices, J. Nucl. Mater. 415 (1) (2011) S2–S9, https://doi.org/10.1016/j.jnucmat.2011.01.110.
[2] M. Kaufmann, R. Neu, Tungsten as first wall material in fusion devices, Fusion Eng. Des. 82 (5-14) (2007) 521–527, https://doi.org/10.1016/j.fusengdes.2007.03.045.
[3] R.A. Causey, Hydrogen isotope retention and recycling in fusion reactor plasma-facing components, J. Nucl. Mater. 300 (2-3) (2002) 91–117, https://doi.org/10.1016/S0022-3115(01)00732-2.
[4] J.W. Coenen, Fusion materials development at Forschungszentrum Jülich, Adv. Eng. Mater. 22 (6) (2020) 1901376, https://doi.org/10.1002/adem.v22.610.1002/adem.201901376.
[5] C. Bachmann, G. Aiello, R. Albanese, R. Ambrosino, F. Arbeiter, J. Aubert, L. V. Boccaccini, D. Carloni, G. Federici, U. Fischer, M.D. Kovari, A. Li-Puma, A. B. Loving, I.A. Maione, M. Mattei, G. Mazzone, B. Meszaros, I. Palermo, P. E. Pereslavtsev, V.T. Riccardo, P. Sardain, N.P. Taylor, R. Villari, Z. Vizvary, A. Vaccaro, E. Visca, R.P. Wenninger, Initial DEMO tokamak design configuration studies, Fusion Eng. Des. 98–99 (2015) 1423–1426, https://doi.org/10.1016/j.fusengdes.2015.05.027.
[6] M. Rieth, M. Schirra, A. Falkenstein, P. Graf, S. Heger, H. Kempe, R. Lindau, H. Zimmermann, EUROFER 97: Tensile, charpy, creep and structural tests. Wissenschaftliche Berichte, FZKA-6911, Karlsruher Institüt für Technologie, Karlsruhe, 2003.
[7] B. van der Schaaf, F. Tavassoli, C. Fazio, E. Rigal, E. Diegele, R. Lindau, G. LeMarois, The development of EUROFER reduced activation steel, Fusion Eng. Des. 69 (1-4) (2003) 197–203, https://doi.org/10.1016/S0920-3796(03)00337-5.
[8] R. Lindau, A. Möslang, M. Rieth, M. Klimiankou, E. Materna-Morris, A. Alamo, A.-A.-F. Tavassoli, C. Cayron, A.-M. Lancha, P. Fernandez, N. Baluc, R. Schäublin, E. Diegele, G. Filacchioni, J.W. Rensman, B. Schaaf, E. Lucon, W. Dietz, Present development status of EUROFER and ODS-EUROFER for application in blanket concepts, Fusion Eng. Des. 75–79 (2005) 989–996, https://doi.org/10.1016/j.fusengdes.2005.06.186.
[9] O.K. von Goldbeck, Fe—W Iron—Tungsten, in: O.K. von Goldbeck (Ed.), Iron-Binary Phase Diagrams, Springer, Berlin, Heidelberg, 1982, pp. 164–167.
[10] D. Qu, W.W. Basuki, J. Aktaa, Numerical assessment of functionally graded tungsten/EUROFER coating system for first wall applications, Fusion Eng. Des. 98–99 (2015) 1389–1393, https://doi.org/10.1016/j.fusengdes.2015.06.160.
[11] S. Heuer, T. Weber, G. Pintsuk, J.W. Coenen, J. Matejicek, C. Linsmeier, Aiming at understanding thermo-mechanical loads in the first wall of DEMO: Stress-strain evolution in a Eurofer-tungsten test component featuring a functionally graded

interlayer, Fusion Eng. Des. 135 (2018) 141–153, https://doi.org/10.1016/j.fusengdes.2018.07.011.
[12] T. Weber, J. Aktaa, Numerical assessment of functionally graded tungsten/steel joints for divertor applications, Fusion Eng. Des. 86 (2-3) (2011) 220–226, https://doi.org/10.1016/j.fusengdes.2010.12.084.
[13] J. Matejicek, H. Boldyryeva, V. Brozek, P. Sachr, T. Chraska, Z. Pala, W–steel and W-WC–steel composites and FGMs produced by hot pressing, Fusion Eng. Des. 100 (2015) 364–370, https://doi.org/10.1016/j.fusengdes.2015.06.154.
[14] D. Qu, Z. Zhou, J. Tan, J. Aktaa, Characterization of W/Fe functionally graded materials manufactured by resistance sintering under ultra-high pressure, Fusion Eng. Des. 91 (2015) 21–24, https://doi.org/10.1016/j.fusengdes.2014.12.014.
[15] M. Koller, A. Kruisova, R. Musalek, J. Matejicek, H. Seiner, M. Landa, On the relation between microstructure and elastic constants of tungsten/steel composites fabricated by spark plasma sintering, Fusion Eng. Des. 133 (2018) 51–58, https://doi.org/10.1016/j.fusengdes.2018.05.056.
[16] C. Tan, G. Wang, L. Ji, Y. Tong, X.-M. Duan, Investigation on 316L/W functionally graded materials fabricated by mechanical alloying and spark plasma sintering, J. Nucl. Mater. 469 (2016) 32–38, https://doi.org/10.1016/j.jnucmat.2015.11.024.
[17] V. Mamedov, Spark plasma sintering as advanced PM sintering method, Powder Metall. 45 (4) (2002) 322–328, https://doi.org/10.1179/003258902225007041.
[18] R.D. Wilson, Explore the potential of capacitor-discharge welding, Adv. Mater. Process. 145 (1994) 93–94.
[19] K. Okazaki, D.K. Kim, H.R. Pak, in: Rapidly Solidified Materials, Properties and Processing, ASM International, Metals Park, Ohio, 1988, p. 183.
[20] K. Okazaki, D.K. Kim, K. Ogata, in: Advances in Powder Metallurgy, Metal Powder Industries Federation, Princeton, New Jersey, 1989, p. 317.
[21] J. Qiu, T. Shibata, C. Rock, K. Okazaki, Electro-discharge consolidation of atomized high strength aluminum powders, Mater. Trans. 38 (3) (1997) 226–231, https://doi.org/10.2320/matertrans1989.38.226.
[22] P. Schütte, J. Garcia, W. Theisen, Electro discharge sintering as a process for rapid compaction in PM-Technology, in: Proceedings EURO PM2009, Copenhagen, Denmark, 2009, pp. 91–99.
[23] L. Leich, A. Röttger, W. Theisen, M. Krengel, Densification of nanocrystalline NdFeB magnets processed by electro-discharge sintering: Microstructure, magnetic, and mechanical properties, J. Magn. Magn. Mater. 460 (2018) 454–460, https://doi.org/10.1016/j.jmmm.2018.04.035.
[24] S. Heuer, T. Lienig, A. Mohr, T. Weber, G. Pintsuk, J.W. Coenen, F. Gormann, W. Theisen, C. Linsmeier, Ultra-fast sintered functionally graded Fe/W composites for the first wall of future fusion reactors, Compos. B. Eng. 164 (2019) 205–214, https://doi.org/10.1016/j.compositesb.2018.11.078.
[25] P. Schütte, Aufbau einer Kurzzeitsinteranlage zur Herstellung verschleißbeständiger Verbundwerkstoffe, Ruhr Universität-Bochum, Bochum, Germany, 2013. PhD dissertation.
[26] A. Mohr, A. Röttger, M. Windmann, W. Theisen, Rezyklieren von metallischen Spänen mittels Electro-Discharge Sintering, Mat.-wiss. u. Werkstofftech 45 (6) (2014) 552–560, https://doi.org/10.1002/mawe.201400266.
[27] S. Heuer, Charakterisierung gradierter Eisen/Wolfram-Schichten für die erste Wand von Fusionsreaktoren, Ruhr Universität-Bochum, Bochum, Germany, 2017. PhD dissertation.
[28] L. Leich, A. Röttger, R. Kuchenbecker, W. Theisen, Electro-discharge sintering of nanocrystalline NdFeB magnets: process parameters, microstructure, and the resulting magnetic properties, J. Mater. Sci.: Mater Electron 31 (22) (2020) 20431–20443, https://doi.org/10.1007/s10854-020-04562-6.
[29] L. Leich, A. Röttger, M. Krengel, W. Theisen, Recycling of NdFeB magnets by electrodischarge sintering—microstructure, magnetic, and mechanical properties, J. Sustain. Metall. 5 (1) (2019) 107–117, https://doi.org/10.1007/s40831-018-0204-2.
[30] R. Orrù, R. Licheri, A.M. Locci, A. Cincotti, G. Cao, Consolidation/synthesis of materials by electric current activated/assisted sintering, Mater. Sci. Eng. R Rep. 63 (4-6) (2009) 127–287, https://doi.org/10.1016/j.mser.2008.09.003.
[31] O. Guillon, J. Gonzalez-Julian, B. Dargatz, T. Kessel, G. Schierning, J. Räthel, M. Herrmann, Field-Assisted Sintering Technology/Spark Plasma Sintering: mechanisms, materials, and technology developments, Adv. Eng. Mater. 16 (7) (2014) 830–849, https://doi.org/10.1002/adem.201300409.
[32] T. Alp, M. Can, S.T.S. Al-Hassani, Electroimpact compaction of PM components, Powder Metall. 30 (1) (1987) 29–36, https://doi.org/10.1179/pom.1987.30.1.29.
[33] S. Clyens, S.T.S. Al-Hassani, W. Johnson, The compaction of powder metallurgy bars using high voltage electrical discharges, Int. J. Mech. Sci. 18 (1) (1976) 37–40, https://doi.org/10.1016/0020-7403(76)90073-4.
[34] ASTM Standard D30, Standard test method for flexural properties of polymer matrix composite materials, ASTM International, West Conshohocken, PA.
[35] K.D. Zilnyk, V.B. Oliveira, H.R.Z. Sandim, A. Möslang, D. Raabe, Martensitic transformation in Eurofer-97 and ODS-Eurofer steels: A comparative study, J. Nucl. Mater. 462 (2015) 360–367, https://doi.org/10.1016/j.jnucmat.2014.12.112.
[36] S. Saroja, M. Vijayalakshmi, V.S. Raghunathan, Influence of cooling rates on the transformation behaviour of 9Cr-1 Mo-0.07C steel, J. Mater. Sci. 27 (9) (1992) 2389–2396, https://doi.org/10.1007/BF01105048.
[37] ITER, Materials Properties Hanbook (MPH): ITER Doc. G74 MA 16 04-05-07 R0.1., 2017.
[38] EUROFUSION, DEMO Material Property Handbook (MPH): EUROFER 97.
[39] S. Heuer, J.W. Coenen, G. Pintsuk, J. Matejicek, M. Vilemova, C. Linsmeier, Overview of challenges and developments in joining tungsten and steel for future

fusion reactors, Phys. Scr. T171 (2020) 14028, https://doi.org/10.1088/1402-4896/ab47a4.

[40] T. Weber, Entwicklung und Optimierung von gradierten Wolfram/EUROFER97-Verbindungen für Divertorkomponenten, Karlsruher Institüt für Technologie, Karlsruhe, Germany, 2013. PhD dissertation.

[41] S. Raju, B.J. Ganesh, A. Banerjee, E. Mohandas, Characterisation of thermal stability and phase transformation energetics in tempered 9Cr–1Mo steel using drop and differential scanning calorimetry, Mater. Sci. Eng. A 465 (1-2) (2007) 29–37, https://doi.org/10.1016/j.msea.2007.01.127.